P^2INR-FWI: an Implicit Neural Representation Method for Speed of Sound Image Reconstruction in Ultrasound Computed Tomography

Zesong Wang[1,2], Weicheng Yan[1,2], Zhaohui Liu[1,2], Ming Yuchi[1,2], and Wu Qiu[1,2]⋆

[1] College of Life Science and Technology, Huazhong Science of Science and Technology, Hubei, China
[2] Advanced Biomedical Imaging Facility, Hubei, China

Abstract. Ultrasound Computed Tomography (USCT) has emerged as a cutting-edge imaging modality, offering quantitative acoustic parameter maps to enhance disease diagnosis. Full-waveform Inversion (FWI), a mainstream reconstruction method, enables high-resolution imaging of the speed of sound (SOS) from USCT measurements. However, its strong sensitivity to the initial model and the anatomical distortions caused by cycle-skipping artifacts significantly hinder its application in complex clinical scenarios. In this paper, we propose P^2INR-FWI, a Polar coordinate-based Implicit Neural Representation framework with structural Prior, to achieve unsupervised, subject-specific SOS reconstruction. Departing from conventional Cartesian coordinate-based neural representations, our method introduces a polar coordinate encoding mechanism aligned with the geometry of the USCT ring array, which substantially accelerates convergence and improves reconstruction accuracy. Furthermore, we develop a reflected signal-derived structural prior extraction method to guide the reconstruction process toward clinically critical regions, thereby enabling fine-structure restoration. Experiments conducted on numerical phantom, breast-mimicking phantom, and in vivo data demonstrate that our method outperforms traditional approaches in both reconstruction quality and quantitative metrics, without requiring additional regularization constraints.

Keywords: Implicit Neural Representation · Ultrasound imaging · Speed of sound imaging

1 Introduction

Breast tissue composition varies across populations, with Asian women having higher breast density, a known risk factor for breast cancer [3]. Moreover, the incidence of breast cancer in Asian women is rising, particularly among younger women [9], highlighting the need for improved diagnostic techniques. Ultrasound

---

⋆ Corresponding Author: wuqiu@hust.edu.cn(Wu Qiu)

Computed Tomography (USCT) combines the non-invasive, radiation-free benefits of traditional ultrasound with improved imaging depth and resolution, making it a promising medical imaging technique, particularly for applications like breast cancer screening [6]. Speed of sound (SOS) imaging, a quantitative mapping technique in USCT, plays a crucial role in assisting breast cancer diagnosis [6,18]. Traditional SOS reconstruction methods, like ray-based time-of-flight [10], are limited in resolution, while Full-Waveform Inversion (FWI) [4] enables higher precision by fully utilizing wavefield data. However, FWI's computational intensity, sensitivity to initial models and susceptibility to cycle-skipping artifacts [7], pose challenges for clinical use.

To overcome these issues, various strategies have been proposed, including improved regularization constraints (e.g., optimal transport metrics [24], learned regularization [21]) and parameter space expansion [14]. However, these approaches often suffer from limited effectiveness or increased computational complexity. Recently, deep learning has opened new avenues, with data-driven methods such as InversionNet [25] and GAN-FWI [13]. Additionally, CNN-based architectures have successfully enabled end-to-end mapping from wavefield data to SOS images [12], although the scarcity of medical imaging data limits their generalization. Physics-informed neural networks (PINNs), integrating prior knowledge from partial differential equations, show potential for solving inverse problems. Initial attempts have applied PINNs to FWI [16]. Building on these ideas, the PEN-FWI model was proposed for ultrasound brain imaging [17], but its generalization is constrained by the slice-specific nature of the training data.

Implicit Neural Representation (INR), a novel deep learning paradigm, has shown strong capabilities in medical image reconstruction, including CT and MRI [19,26]. INR has also been combined with differentiable beamforming to estimate sound speed distributions and assist B-mode image reconstruction [5]. However, its integration with FWI for high-resolution SOS imaging in USCT remains unexplored. To address these challenges, we propose P^2INR-FWI, an INR framework combining Polar-based radial-angular coordinate embedding (RACE) and structural Prior, trained in an unsupervised and subject-specific manner. Our contributions are three-fold: 1) We propose a novel INR framework for designed USCT that effectively mitigates cycle-skipping and reduces reliance on the initial model. 2) A radial-angular coordinate-based position encoding strategy is introduced, tailored to the ring-shaped USCT sensor array, enhancing both training convergence and reconstruction accuracy. 3) We develop a structural prior extraction algorithm using reflected signals, which guides training with anatomical priors, thereby boosting reconstruction efficiency and accuracy.

2 Methodology

2.1 Preliminaries

FWI is an optimization technique constrained by wave equations. Assuming a non-dissipative and isotropic medium where wave propagation occurs, the acoustic pressure p adheres to the standard wave equation.

$$\frac{1}{c(\mathbf{x})^2}\frac{\partial^2 p(\mathbf{x},t)}{\partial t^2} - \Delta p(\mathbf{x},t) = s(\mathbf{x},t), \quad (\mathbf{x},t) \in \mathbb{R}^2 \times [0,T] \tag{1}$$

Guided by the wave equation, the speed of sound is estimated by minimizing the mismatch between the simulated and observed data.

$$\hat{c} = arg\,\underset{c}{min}\sum_{i}^{N_s}\sum_{j}^{N_r}\|p_{obs}(i,j) - p_{sim}(i,j,c)\|_2, \quad p_{sim}(c) = \mathbf{R}\cdot p(c), \tag{2}$$

where $p_{obs} \in \mathbb{R}^{N_s \times N_r \times T}$ represents the observed data collected by the USCT system, N_s denotes the number of transmitting sound sources, N_r indicates the number of receiving sensors, and T corresponds to the number of sampling time points. p_{sim} refers to the simulated acoustic pressure data, and the sampling operator $\mathbf{R}$ represents the locations of the receiving sensors.

As a non-convex, ill-posed inverse problem, FWI faces inherent challenges, especially in medical ultrasound. It is highly sensitive to the initial model and noise, and its nonlinear nature increases algorithmic complexity. Additionally, cycle-skipping artifacts, caused by wavefield phase ambiguities, often trap optimizations in local minima, leading to anatomically inconsistent reconstructions.

2.2 Proposed P^{2}INR-FWI Framework

To tackle the challenges in FWI, we propose P^{2}INR-FWI, an implicit neural representation framework incorporating structural prior and polar-based radial-angular coordinate encoding. The method establishes an implicit mapping between spatial coordinates and speed of sound values through neural network parameters, providing implicit regularization that not only mitigates cycle-skipping artifacts but also reduces FWI's sensitivity to initial models and noise.

A. Framework Overview: As shown in Fig. 1, our architecture contains four key components: 1) Polar Coordinate Encoding: Transform Cartesian coordinates to radial-angular parameters with Fourier feature embedding; 2) Implicit SOS Mapping: Position-to-value regression via MLP network; 3) Anatomical Prior Guidance: Apply structural mask to constrain background with known SOS values; 4) Physics-informed Optimization: Forward-modeled wavefield comparison for network updating.

Our network architecture is based on SIREN [20]. The MLP model consists of 5 fully connected layers, with a $sine(\cdot)$ activation function applied after each layer except the final one, which uses a $Sigmoid(\cdot)$ activation function for output normalization. The network initialization follows the recommended scheme from the original SIREN implementation. The network includes 4 hidden layers, each containing 512 neurons. The loss function comprises data consistency (DC) and regularization terms, including total variation (TV) and structural prior regularization:

$$\mathcal{L} = \mathcal{L}_{DC} + \alpha\mathcal{L}_{TV} + \beta\mathcal{L}_{prior} \tag{3}$$

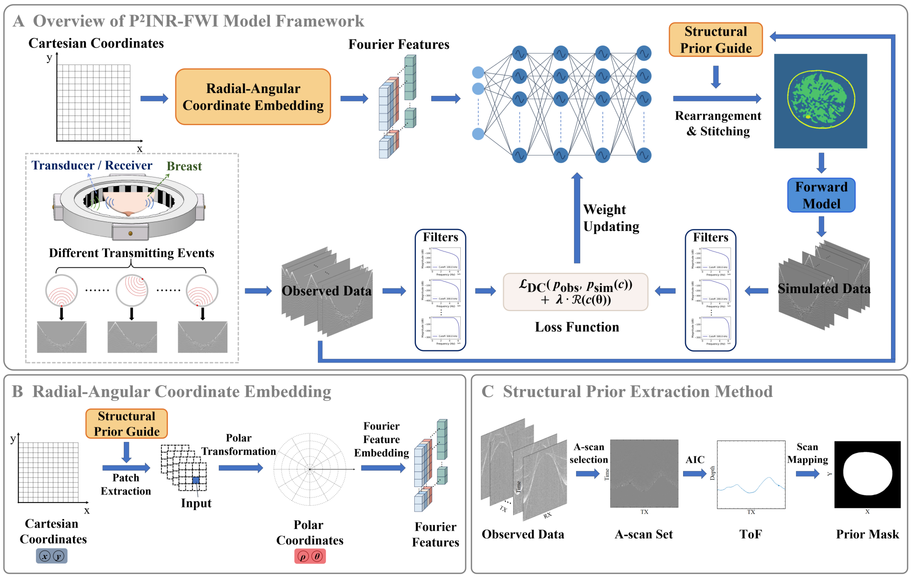

Fig. 1. Overview of our proposed P^{2}INR-FWI Model framework.

where α and β are the weighting parameters for TV and structural prior losses, respectively. The terms are defined as:

$$\mathcal{L}_{DC} = \|p_{obs} - \mathrm{N}_R(\hat{c})\|_2,\ \mathcal{L}_{TV} = \iint \sqrt{\hat{c}_x^2 + \hat{c}_y^2}\, dxdy,\ \mathcal{L}_{prior} = \|\mathbf{M} \odot (\hat{c} - c_b)\|_2 \quad (4)$$

where $\mathrm{N}_R(\cdot)$ represents the forward physical model to convert the SOS image to the signal, $\hat{c}$ is the predicted SOS image, $\mathbf{M}$ is a mask that identifies the background region, and c_b represents the known background SOS value.

B. Radial-Angular Coordinate Embedding (RACE): Existing INR methods primarily employ Cartesian coordinates or their encoded variants for medical image reconstruction [19,26], neglecting USCT's physical characteristics. The circular transducer array creates radially distributed wavefronts with angular sampling sparsity, while anatomical targets typically exhibit central-peripheral structural organization. Our Radial-Angular Coordinate Embedding (RACE) directly addresses these USCT-specific features through polar coordinate parameterization, adapting to the sparsity of angular sampling through θ-axis.

The Cartesian coordinates $v = [x, y]$ are first converted to polar parameters $p = [\rho, \theta]$ centered at the imaging region's center:

$$\rho = \sqrt{(x - x_0)^2 + (y - y_0)^2}, \quad \theta = \arctan \frac{y - y_0}{x - x_0} \quad (5)$$

where ρ denotes the radial distance and θ the angular coordinate. The vector $v_0 = [x_0, y_0]$ represents the pole, the center of the image.

We perform Fourier feature embedding to transform the polar coordinates into a higher-dimensional feature space, enabling the network to learn high-frequency details more effectively [22]. This is achieved through a randomly generated Gaussian matrix $\mathrm{B} \in \mathbb{R}^{\frac{d}{2}\times 2}$, where d controls the feature vector's dimensionality. Each entry in B is sampled independently from a normal distribution $\mathcal{N}(0,\sigma^2)$, and the feature vectors are computed as follows:

$$\gamma(p) = [\cos(2\pi \mathrm{B}p), \sin(2\pi \mathrm{B}p)]^{\mathrm{T}} \tag{6}$$

In this case, we set d to 1000 and σ to 0.1.

RACE is well-suited for USCT data representation, enriching spatial information and improving the model's ability to capture fine details.

C. Structural Prior Extraction: We utilize reflected signals to derive structural prior information for anatomical contour delineation. During USCT signal acquisition, a coupling agent with known sound speed provides a priori information for regions external to the anatomy, enabling generation of a mask that defines region-of-interest (ROI) boundaries.

First, the signals from the transmit element itself in each transmit event are extracted from the observed data p_{obs}, forming the A-scan data set $A \in \mathbb{R}^{N_s \times T}$. The Akaike Information Criterion (AIC) method [2] is then applied to identify first-arrival times in each A-scan signal. The AIC method assumes the signal has two locally stationary segments: one before and one after the first-arrival time, and identifies the first-arrival time k by minimizing the following equation:

$$AIC(k) = k \log \sigma^2_{1:k} + (T-k)\log \sigma^2_{k+1:T} \tag{7}$$

where $\sigma^2_{1:k}$ and $\sigma^2_{k+1:T}$ are the variances of the two segments, with T representing time samples. The distance between the boundary and the corresponding transmit array is determined by multiplying half of the first-arrival time by the coupler's sound speed. Finally, coordinate transformation converts these distance measurements into Cartesian space for boundary reconstruction.

3 Experiments and Results

3.1 Experiment Settings

A. Datasets: In this study, we carried out experiments using numerical phantom (ground truth derived from MRI segmentation dataset [11]), real breast phantom, and in vivo breast tissue data to assess the proposed method. Numerical data were simulated using 500 kHz Ricker wavelets with 256 uniformly distributed circular transducers (64 transmitters), and random Gaussian noise was added to achieve a signal-to-noise ratio (SNR) of 40 dB, thereby simulating real-world conditions. The real breast phantom (Fig. 3(a)) mimicked the shape of a human breast, containing a 3 mm cylindrical insert (1580 ± 10 m/s) within a 1540 ± 10 m/s main body. In vivo data were acquired from two volunteers with distinct glandular and fat tissue distributions. Both phantom and in vivo data

were collected using our custom system (512 sensors, 500 kHz center frequency, 25 kHz sampling rate), with 256 transmitters for phantoms and 512 for in vivo.
B. Evaluation Metrics: We used classical least-squares-based Full-Waveform Inversion (FWI) as the baseline method. In numerical experiments, we compared six approaches: FWI, mFWI (FWI with multi-frequency strategy), INR-FWI, INR-mFWI, P^{2}INR-FWI, and P^{2}INR-mFWI. For phantom and in vivo experiments, we adopted mFWI, INR-mFWI and P^{2}INR-mFWI due to their superior robustness. Quantitative evaluations utilized four metrics: Structural Similarity Index (SSIM) [23], Peak Signal-to-Noise Ratio (PSNR), Root Mean Square Error (RMSE), and Learned Perceptual Image Patch Similarity (LPIPS) [27].
C. Implementation Details: All methods initialized with a known homogeneous background SOS model. We trained separate models for each data scenario using PyTorch [15] and the Adam optimizer [8], with an initial learning rate of $1e^{-4}$. For numerical simulation, the learning rate decayed by 0.8 every 500 epochs, totaling 6000 epochs. For phantom and in vivo data, it decayed every 200 epochs, totaling 600 epochs. The coefficients were fixed at $\beta = 1e^{-5}$ throughout, with $\alpha = 0$ (numerical simulation) or $2e^{-5}$ (phantom and in vivo), empirically validated. All experiments utilized an NVIDIA RTX 4090 GPU.

3.2 Results

We defined a square computational domain of 0.23 m per side for all experiments. Numerical experiments lasted 0.2 ms, while phantom and in vivo experiments lasted 0.16 ms. A uniformly distributed circular array of ultrasound sensors with a diameter of 0.22 m was used for signal transmission and data acquisition.

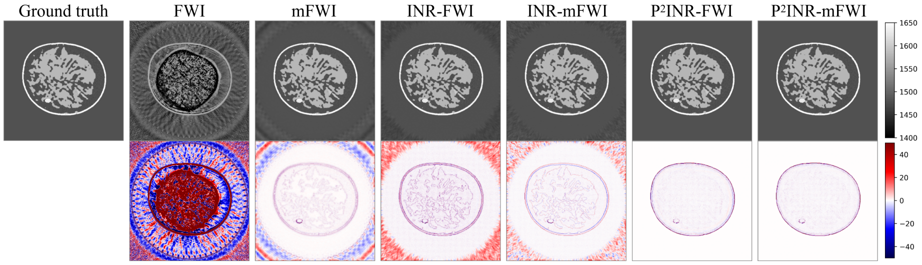

Fig. 2. Reconstruction performance comparison in numerical experiment.

A. Numerical Experiment: To satisfy the Courant-Friedrichs-Lewy condition [1], we discretized the computational domain into a 592×592 grid with 3000 time steps for forward modeling using the finite difference method. We employed classical FWI as the baseline and compared the performance of six approaches. Quantitative evaluation results are presented in Tab. 1, and experimental results, with reconstruction images above and misfit maps below, are shown in

Fig.2. mFWI applies a multi-frequency strategy to FWI by using low-pass Butterworth filters with cutoff frequencies of 100, 200, 300, 400, and 500 kHz to separate the data into distinct frequency bands, mitigating the cycle-skipping effect. Our method excels in both metrics and visual quality, achieving competitive performance even without the multi-frequency strategy.

Table 1. Quantitative results on the numerical phantom.

Methods	SSIM ↑	PSNR ↑	RMSE ↓	LPIPS ↓
FWI	0.695	23.358	65.870	0.733
mFWI	0.904	32.603	5.066	0.329
INR-FWI	0.906	29.193	6.135	0.291
INR-mFWI	0.912	32.820	4.562	0.305
P^{2}INR-FWI	0.986	34.289	4.284	0.053
P^{2}INR-mFWI	0.986	34.271	4.220	0.053

B. Breast Phantom Experiment: In the breast phantom experiment, we employed an 896×896 grid discretization with 3956 time steps for wave propagation modeling, incorporating water coupling during data acquisition. As shown in Fig.3, while all methods successfully resolve the high-speed cylindrical target, mFWI exhibits sound speed underestimation manifesting as a low-velocity artifact at the breast-water interface; INR-FWI demonstrates systematic overestimation attributed to insufficient prior information constraints. Notably, detailed analysis of a subregion adjacent to the target in Fig.3(e) demonstrates our method's superior reconstruction accuracy relative to the ground truth.

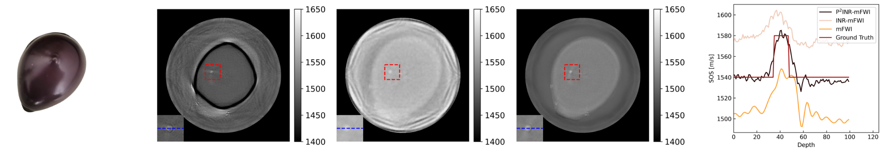

(a) Breast Phantom (b) mFWI (c) INR-mFWI (d) P^{2}INR-mFWI (e) SOS Comparison

Fig. 3. Breast phantom reconstruction. Profiles in (e) show SOS values along the lines marked in (b), (c) and (d) at y = 109 mm for ground truth and method results.

C. In vivo Experiment: For in vivo experiment, we employed an 896×896 spatial grid with 4356 temporal steps. A solid gel coupling agent (SGCA) [28] was used as the coupling medium. Fig. 4 presents the reconstruction results, where (a) and (b) correspond to two different subjects.

D. Ablation Study: To validate the effectiveness of our method's core components, we incrementally integrated each module into the FWI framework. "Base"

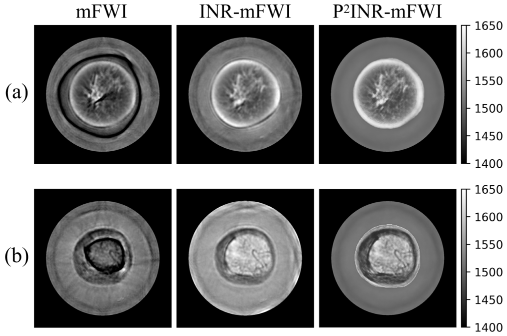

Fig. 4. In vivo reconstruction results.

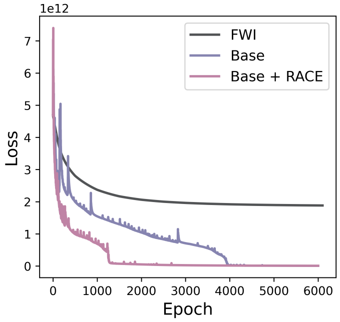

Fig. 5. Loss curve comparisons on numerical phantom.

refers to the INR-based FWI reconstruction, the foundational framework for our approach. Ablation studies on the numerical phantom in Tab. 2 confirm that all components collectively improve reconstruction accuracy, with the structural prior specifically enhancing final precision. Training loss curves (see Fig. 5) further demonstrate the RACE module's role in accelerating convergence. Numerical simulations indicate that although our method requires 7.1 s per iteration (vs. 5.6 s for conventional FWI) with more iterations needed for converge, it achieves significantly improved reconstruction accuracy. Notably, incorporating structural prior into classical FWI failed to resolve cycle-skipping, yielding poor reconstruction results.

Table 2. Ablation Study Results on the contributed components.

Base	RACE	Prior	SSIM ↑	PSNR ↑	RMSE ↓	LPIPS ↓
×	×	×	0.695	23.358	65.870	0.733
×	×	✓	0.770	23.552	71.524	0.497
✓	×	×	0.906	29.193	6.135	0.291
✓	✓	×	0.929	32.046	5.540	0.258
✓	×	✓	0.984	34.167	4.335	0.054
✓	✓	✓	**0.986**	**34.289**	**4.284**	**0.053**

4 Discussion and Conclusion

Our work proposes an INR-based Full-waveform Inversion method for USCT, aimed at high-resolution SOS reconstruction. To address the ring-array acquisition geometry of USCT system, we develop a radial-angular coordinate embedding (RACE) strategy, demonstrating enhanced convergence and accuracy over Cartesian coordinate-based approaches. A structural prior extraction algorithm is further designed based on reflected signals, and anatomical features are integrated into the training process, significantly improving reconstruction reliability. The abrupt loss drop stems from the network's outward-to-inward learning tendency induced by sparse simulation data, where persistent central gaps suddenly resolve into complete structures during convergence.

Our method establishes a subject-specific self-supervised training paradigm, leveraging the network's implicit regularization to reduce the dependence on the initial model and effectively mitigate the cycle-skipping problem in traditional FWI. Experimental results show that it significantly improves the quality of USCT speed of sound image, providing more reliable imaging support for breast disease diagnosis.

Acknowledgement. The authors are grateful to the High-Performance Computing platform of Huazhong University of Science and Technology and the Supercomputing Platform of Hubei Medical Devices Quality Supervision and Test Institute.

Disclosure of Interests. The authors have no competing interests to declare that are relevant to the content of this article.

References

1. Abe, K., Higashimori, N., Kubo, M., Fujiwara, H., Iso, Y.: A remark on the courant-friedrichs-lewy condition in finite difference approach to pde's. Advances in Applied Mathematics and Mechanics **6**(5), 693–698 (2014)
2. Akaike, H.: A new look at the statistical model identification. IEEE Transactions on Automatic Control **19**(6), 716–723 (1974)
3. Bae, J.M., Kim, E.H.: Breast density and risk of breast cancer in asian women: A meta-analysis of observational studies. Journal of Preventive Medicine and Public Health **49**(6), 367–375 (2016)
4. Bernard, S., Monteiller, V., Komatitsch, D., Lasaygues, P.: Ultrasonic computed tomography based on full-waveform inversion for bone quantitative imaging. Physics in Medicine & Biology **62**(17), 7011–7035 (2017)
5. Byra, M., Jarosik, P., Karwat, P., Klimonda, Z., Lewandowski, M.: Implicit neural representations for speed-of-sound estimation in ultrasound. 2024 IEEE Ultrasonics, Ferroelectrics, and Frequency Control Joint Symposium (UFFC-JS) pp. 1–4 (2024)
6. Duric, N., Littrup, P., Poulo, L., Babkin, A., Pevzner, R., Holsapple, E., Rama, O., Glide, C.: Detection of breast cancer with ultrasound tomography: First results with the computed ultrasound risk evaluation (cure) prototype. Medical physics **34**(2), 773–785 (2007)
7. Hu, W., Chen, J., Liu, J., Abubakar, A.: Retrieving low wavenumber information in fwi: An overview of the cycle-skipping phenomenon and solutions. IEEE Signal Processing Magazine **35**(2), 132–141 (2018)
8. Kingma, D.P., Ba, J.: Adam: A method for stochastic optimization. arXiv preprint arXiv:1412.6980 (2014)

9. Lei, S., Zheng, R., Zhang, S., Wang, S., Chen, R., Sun, K., Zeng, H., Zhou, J., Wei, W.: Global patterns of breast cancer incidence and mortality: A population-based cancer registry data analysis from 2000 to 2020. Cancer Communications **41**(11), 1183–1194 (2021)
10. Li, C., Duric, N., Littrup, P., Huang, L.: In vivo breast sound-speed imaging with ultrasound tomography. Ultrasound in Medicine & Biology **35**(10), 1615–1628 (2009)
11. Lou, Y., Zhou, W., Matthews, T., Appleton, C., Anastasio, M.: Generation of anatomically realistic numerical phantoms for photoacoustic and ultrasonic breast imaging. Journal of biomedical optics **22** (2017)
12. Lozenski, L., Wang, H., Li, F., Anastasio, M., Wohlberg, B., Lin, Y., Villa, U.: Learned full waveform inversion incorporating task information for ultrasound computed tomography. IEEE Transactions on Computational Imaging **10**, 69–82 (2024)
13. Mosser, L., Dubrule, O., Blunt, M.J.: Stochastic seismic waveform inversion using generative adversarial networks as a geological prior. Mathematical Geosciences **52**, 53–79 (2020)
14. Operto, S., Gholami, A., Aghamiry, H.S., Guo, G., Mamfoumbi, F., Beller, S.: Full waveform inversion beyond the born approximation: A tutorial review. arXiv preprint arXiv:2212.10141 (2022)
15. Paszke, A., Gross, S., Massa, F., Lerer, A., Bradbury, J., Chanan, G., Killeen, T., Lin, Z., Gimelshein, N., Antiga, L., et al.: Pytorch: An imperative style, high-performance deep learning library. In: Advances in Neural Information Processing Systems. vol. 32 (2019)
16. Rasht-Behesht, M., Huber, C., Shukla, K., Karniadakis, G.E.: Physics-informed neural networks (pinns) for wave propagation and full waveform inversions. Journal of Geophysical Research: Solid Earth **127**(5), e2021JB023120 (2022)
17. Ren, J., Li, J., Liu, C., Chen, S., Liang, L., Liu, Y.: Deep learning with physics-embedded neural network for full waveform ultrasonic brain imaging. IEEE Transactions on Medical Imaging **43**(6), 2332–2346 (2024)
18. Sandhu, G.Y., Li, C., Roy, O., Schmidt, S., Duric, N.: Frequency domain ultrasound waveform tomography: breast imaging using a ring transducer. Physics in Medicine & Biology **60**(14), 5381–5398 (2015)
19. Shen, L., Pauly, J., Xing, L.: Nerp: Implicit neural representation learning with prior embedding for sparsely sampled image reconstruction. IEEE Transactions on Neural Networks and Learning Systems **35**(1), 770–782 (2024)
20. Sitzmann, V., Martel, J., Bergman, A., Lindell, D., Wetzstein, G.: Implicit neural representations with periodic activation functions. In: Advances in Neural Information Processing Systems. vol. 33, pp. 7482–7493 (2020)
21. Sun, P., Yang, F., Liang, H., Ma, J.: Full-waveform inversion using a learned regularization. IEEE Transactions on Geoscience and Remote Sensing **61**, 1–15 (2023)
22. Tancik, M., Srinivasan, P.P., Mildenhall, B., Fridovich-Keil, S., Raghavan, N., Singhal, U., Ramamoorthi, R., Barron, J., Ng, R.: Fourier features let networks learn high frequency functions in low dimensional domains. In: Advances in Neural Information Processing Systems. vol. 33, pp. 7537–7547 (2020)
23. Wang, Z., Bovik, A.C., Sheikh, H.R., Simoncelli, E.P.: Image quality assessment: from error visibility to structural similarity. IEEE Transactions on Image Processing **13**(4), 600–612 (2004)
24. Wang, Z., Xiao, J., Li, D., Li, B., Zhang, J., Ta, D.: Full waveform inversion guided wave tomography with a recurrent neural network. Ultrasonics **133**, 107043 (2023)

25. Wu, Y., Lin, Y.: Inversionnet: An efficient and accurate data-driven full waveform inversion. IEEE Transactions on Computational Imaging **6**, 419–433 (2019)
26. Zhang, M., Feng, R., Li, Z., Feng, J., Wu, Q., Zhang, Z., Ma, C., Wu, J., Yan, F., Liu, C., Zhang, Y., Wei, H.: A subject-specific unsupervised deep learning method for quantitative susceptibility mapping using implicit neural representation. Medical Image Analysis **95**, 103173 (2024)
27. Zhang, R., Isola, P., Efros, A.A., Shechtman, E., Wang, O.: The unreasonable effectiveness of deep features as a perceptual metric. In: Proceedings of the IEEE Conference on Computer Vision and Pattern Recognition. pp. 586–595 (2018)
28. Zhou, L., Zhang, Q., Wu, Y., Liu, Z., Wu, Y., Li, X., Qiu, W., Lou, C., Ding, M., Yuchi, M.: A coupling, stabilizing, and shaping strategy for breast ultrasound computed tomography (usct) with a ring array transducer. Ultrasonics **138**, 107212 (2024)